

Chapter 1: Micro-Macro Transition for Cohesive Granular Media

S. LUDING AND H. J. HERRMANN
Institut für Computeranwendungen 1,
Universität Stuttgart
Pfaffenwaldring 27
70569 Stuttgart

1.1 Introduction

A basic question in mechanics and physics is how to bridge the gap between a microscopic model and a macroscopic (continuum) description. The former involves contact forces and deformations, whereas the latter concerns tensorial quantities like the stress or the deformation gradient.

The macroscopic balance equations for mass, momentum and energy can be used for the continuum modeling of the behavior of granular media. However, in order to close the system of equations, they rely on constitutive relations between the physical quantities (expressed in terms of material parameters [8, 13]), since the microscopic details of a granular material are not directly taken into account on the macro-scale. The aim of this paper is to present a micro-macro transition from “microscopic” simulations to macroscopic constitutive relations for the material behavior.

The model system, a two-dimensional bi-axial box filled with cohesive, frictionless disks of different sizes, is examined by means of a “microscopic” discrete element method (DEM). The microscopic interaction model for cohesion is tested via several stress- or strain-controlled bi-axial deformation paths.

Using the whole box as representative elementary volume, the stress is examined as a function of the applied strain, and the yield surface is determined from bi-axial compression tests. Other measured macroscopic parameters are the Young modulus, the Poisson ratio, the dilatancy angle, the friction angle, and the cohesion.

1.2 Model System

One possibility to obtain information about the material behavior is to perform elementary tests in the laboratory. An alternative are simulations with the discrete element model (DEM) [1–3, 9, 10, 12, 14] and the average over the “microscopic” quantities in some averaging volume. The experiment chosen is the bi-axial box set-up, see Fig. 1.1, where the left and bottom walls are fixed, and stress- or strain-controlled deformation is applied. In the first case both the top and right walls are subject to a predefined pressure, in the second case, the top wall is subject to a defined strain ε_{zz} , and the right wall is subject to

constant pressure p_x . In a typical ‘experiment’, the top wall is slowly shifted downwards while the right wall moves dependent on the force exerted on it by the material in the box. The strain-controlled position of the top wall as function of time t is

$$z(t) = z_f + \frac{z_0 - z_f}{2}(1 + \cos \omega t) \quad \text{with} \quad \varepsilon_{zz} = 1 - \frac{z}{z_0}, \quad (1.1)$$

where the initial and final positions z_0 and z_f can be specified together with the rate of deformation $\omega = 2\pi f$ so that after a half-period $T/2 = 1/(2f)$ the extremal deformation is reached. With other words, the cosine is active for $0 \leq \omega t \leq \pi$. For larger times, the top-wall is fixed and the system can relax. The cosine function is chosen in order to allow for a smooth start-up and finish of the motion so that shocks and inertia effects are reduced, however, the shape of the function is arbitrary as long as it is smooth.

The stress-controlled motion of the side-wall is described by

$$m_x \ddot{x}(t) = F_x(t) - p_x z(t) - \gamma_x \dot{x}(t), \quad (1.2)$$

where m_x is the mass of the wall. Large values of m_x lead to slow adaption, small values allow for a rapid adaption to the actual situation. Three forces are active: (i) the force $F_x(t)$ due to the bulk material, (ii) the force $-p_x z(t)$ due to the external pressure, and (iii) a strong frictional force which damps the motion of the wall so that oscillations are reduced.

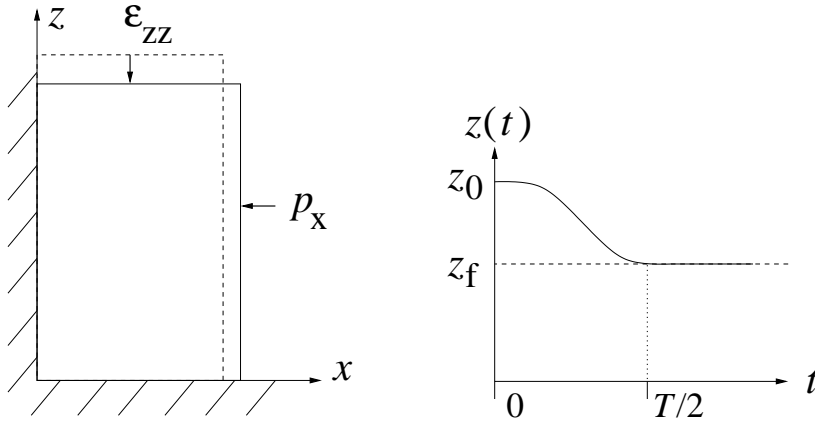


Figure 1.1: (Left) Schematic drawing of the model system. (Right) Position of the top-wall as function of time for the strain-controlled situation.

For small deviations $\xi = x_f - x$ from the equilibrium position x_f , a first order series expansion leads to a damped oscillation $m_x^{\text{eff}} \ddot{\xi} + \gamma_x^{\text{eff}} \dot{\xi} + K_x \xi = 0$, with the stiffness K_x of the material in the horizontal direction, and the eigen-frequency

$$\omega_x = \sqrt{\frac{K_x}{m_x^{\text{eff}}} + \left(\frac{\gamma_x^{\text{eff}}}{2m_x^{\text{eff}}}\right)^2}, \quad (1.3)$$

with the effective mass m_x^{eff} and effective dissipation γ_x^{eff} .

1.3 Discrete Particle Model

The elementary units of granular materials are mesoscopic grains which deform under stress. Since the realistic modeling of the deformations of the particles is much too complicated, we relate the interaction force to the overlap δ of two particles, see Fig. 1.2. Note that the evaluation of the inter-particle forces based on the overlap may not be sufficient to account for the inhomogeneous stress distribution inside the particles. Consequently, our results presented below are of the same quality as the simple assumptions about the force-overlap relation.

If all forces \vec{f}_i acting on the particle i , either from other particles, from boundaries or from external forces, are known, the problem is reduced to the integration of Newton's equations of motion for the translational degrees of freedom

$$m_i \frac{d^2}{dt^2} \vec{r}_i = \vec{f}_i, \quad (1.4)$$

with the mass m_i of particle i , its position \vec{r}_i and the total force $\vec{f}_i = \sum_c \vec{f}_i^c$ acting on it due to contacts with other particles or with the walls. For the sake of simplicity, we neglect tangential forces as well as external forces in the following.

Two particles i and j interact only if they are in contact so that their overlap

$$\delta = \frac{1}{2}(d_i + d_j) - (\vec{r}_i - \vec{r}_j) \cdot \vec{n} \quad (1.5)$$

is positive, $\delta > 0$, with the unit vector $\vec{n} = \vec{n}_{ij} = (\vec{r}_i - \vec{r}_j) / |\vec{r}_i - \vec{r}_j|$ pointing from j to i . The force on particle i , from particle j can be written as $\vec{f}_{ij} = f_{ij} \vec{n}$.

Here we apply a variant of the linear hysteretic spring model [4, 11, 15], as an alternative to the frequently applied spring-dashpot models. This model is the simplest version of some more complicated nonlinear-hysteretic force laws [7, 15, 16] which reflect the fact that at the contact point, plastic deformations may take place. The repulsive (hysteretic) force can be written as

$$f_{ij}^{\text{hys}} = \begin{cases} k_1 \delta & \text{for loading,} & \text{if } k_2(\delta - \delta_0) \geq k_1 \delta \\ k_2(\delta - \delta_0) & \text{for un/reloading,} & \text{if } k_1 \delta > k_2(\delta - \delta_0) > -k_c \delta \\ -k_c \delta & \text{for unloading,} & \text{if } -k_c \delta \geq k_2(\delta - \delta_0) \end{cases} \quad (1.6)$$

with $k_1 \leq k_2$, see Fig. 1.2.

During the initial loading the force increases linearly with the overlap δ , until the maximum overlap δ_{max} is reached (which has to be kept in memory as a history parameter). The line with slope k_1 thus defines the maximum force possible for a given δ . During unloading the force drops from its value at δ_{max} down to zero at overlap $\delta_0 = (1 - k_1/k_2)\delta_{\text{max}}$, on the line with slope k_2 . Reloading at any instant leads to an increase of the force along this line, until the maximum force is reached; for still increasing δ , the force follows again the line with slope k_1 and δ_{max} has to be adjusted accordingly. Unloading below δ_0 leads to negative, attractive forces until at the overlap $\delta_{\text{min}} = \frac{k_2 - k_1}{k_2 + k_c} \delta_{\text{max}}$, the minimum force $-k_c \delta_{\text{min}}$, i.e. the maximum attractive force, is obtained as a function of the model parameters k_1 , k_2 , k_c ,

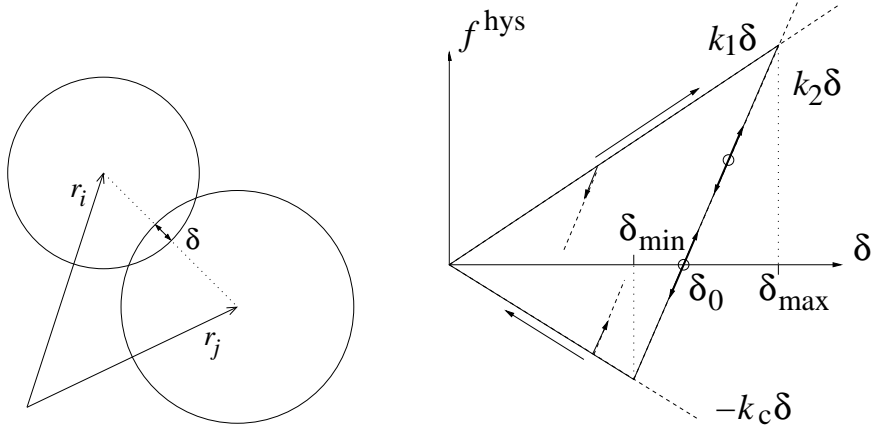


Figure 1.2: (Left) Two particle contact with overlap δ . (Right) Force law for two springs with stiffness k_1 and k_2 for initial loading and subsequent un/reloading, respectively. Attractive forces are possible due to the cohesion strength k_c .

and the history parameter δ_{max} . Further unloading leads to attractive forces $f^{\text{hys}} = -k_c\delta$. The highest possible attractive force, for given k_1 and k_2 , is reached for $k_c \rightarrow \infty$, so that $f_{\text{max}}^{\text{hys}} = -(k_2 - k_1)\delta_{\text{max}}$. This would lead to a discontinuity at $\delta = 0$ what is avoided by using finite k_c .

The lines with slope k_1 and $-k_c$ define the range of possible force values and departure from these lines takes place in the case of unloading and reloading, respectively. Between these two extremes, unloading and reloading follow the same line. Possible equilibrium states are indicated as circles in Fig. 1.2, where the upper and lower circle correspond to a pre-stressed and stress-free state, respectively. In the case of collisions of particles and for large deformations, dissipation takes place due to the hysteretic nature of the force-law. However, for small displacements around some equilibrium state, the model does not contain dissipation. Therefore, in order to allow for stronger dissipation, also a viscous, velocity dependent dissipative force

$$f_{ij}^{\text{diss}} = \gamma_0 \dot{\delta} \quad (1.7)$$

is assumed with some damping coefficient γ_0 . The half-period of a vibration around the equilibrium position, see Fig. 1.2, can be computed for arbitrary values of k_1 and k_c , as long as the overlap fulfills the condition $\delta_{\text{min}} < \delta < \delta_{\text{max}}$, and one obtains a typical response time on the contact level,

$$t_c = \frac{\pi}{\omega}, \quad \text{with} \quad \omega = \sqrt{\frac{k_2}{m_{12}} - \eta_0^2}, \quad (1.8)$$

the eigenfrequency of the contact, and the rescaled damping coefficient $\eta_0 = \gamma_0/(2m_{12})$.

Note that the viscous dissipation takes place in a two-particle contact. In the bulk material, where many particles are in contact with each other, dissipation is very inefficient due to long-wavelength cooperative modes of motion [5, 6]. Therefore, an additional damping

with the background is introduced, so that the total force on particle i is

$$\vec{f}_i = \sum_j (f_{ij}^{\text{hys}} + f_{ij}^{\text{diss}}) \vec{n} - \gamma_b \vec{v}_i, \quad (1.9)$$

with the damping artificially enhanced in the spirit of a rapid equilibration.

1.4 Simulation Results

The systems examined in the following contain $N = 1950$ particles with radii a_i randomly drawn from a homogeneous distribution with minimum $a_{\min} = 0.5 \cdot 10^{-3}$ m and maximum $a_{\max} = 1.5 \cdot 10^{-3}$ m. The masses $m_i = (4/3)\rho\pi a_i^3$, with the density $\rho = 2 \cdot 10^3 \text{ kg m}^{-3}$, are computed as if the particles were spheres. This is an artificial choice and introduces some dispersity in mass in addition to the dispersity in size. However, since we are mainly concerned about slow deformation and equilibrium situations, the choice for the calculation of mass should not matter. The total mass of the particles in the system is thus $M \approx 0.02$ kg with the typical reduced mass of a pair of particles with mean radius, $m_{12} \approx 0.42 \cdot 10^{-5}$ kg. If not explicitly mentioned, the material parameters are $k_2 = 10^5 \text{ N m}^{-1}$ and $\gamma_0 = 0.1 \text{ kg s}^{-1}$. The other spring-constants k_1 and k_c will be defined in units of k_2 . In order to switch on cohesion, $k_1 < k_2$ and $k_c > 0$ is used; in the following, we have $k_1 = k_2/2$.

Using the parameters $k_1 = k_2$ and $k_c = 0$ in Eq. (1.8) leads to a typical contact duration (half-period): $t_c \approx 2.03 \cdot 10^{-5}$ s for $\gamma_0 = 0$, $t_c \approx 2.04 \cdot 10^{-5}$ s for $\gamma_0 = 0.1 \text{ kg s}^{-1}$, and $t_c \approx 2.21 \cdot 10^{-5}$ s for $\gamma_0 = 0.5 \text{ kg s}^{-1}$ for a collision. Accordingly, an integration time-step of $t_{\text{MD}} = 5 \cdot 10^{-7}$ s is used, in order to allow for a ‘safe’ integration of contacts involving smaller particles. Large values of k_c lead to strong cohesive forces, so that also more energy can be dissipated in one collision. The typical response time of the particle pairs, however, is not affected so that the numerical integration works well.

1.4.1 Initial Configuration

Initially, the particles are randomly distributed in a huge box, with rather low overall density. Then the box is compressed, either by moving the walls to their desired position, or by defining an external pressure $p = p_x = p_z$, in order to achieve an isotropic initial condition. Starting from a relaxed, isotropic initial configuration, the strain is applied to the top wall and the response of the system is examined. In Fig. 1.3, the contact network from a typical simulation is shown before compression, at failure and in the final, relaxed state. The dark lines indicate strong contact forces so that the contact network appears denser in the last image due to the deformation and compression. A more quantitative study of the fabric tensor, however, is far from the scope of this study and will be presented elsewhere. Before presenting more detailed results, we have to remark that the initial preparation and set-up of the system is still an open issue to be examined. A possible alternative to the approach used here is the preparation of the system in a critical flow state, which should not depend on the history any more.

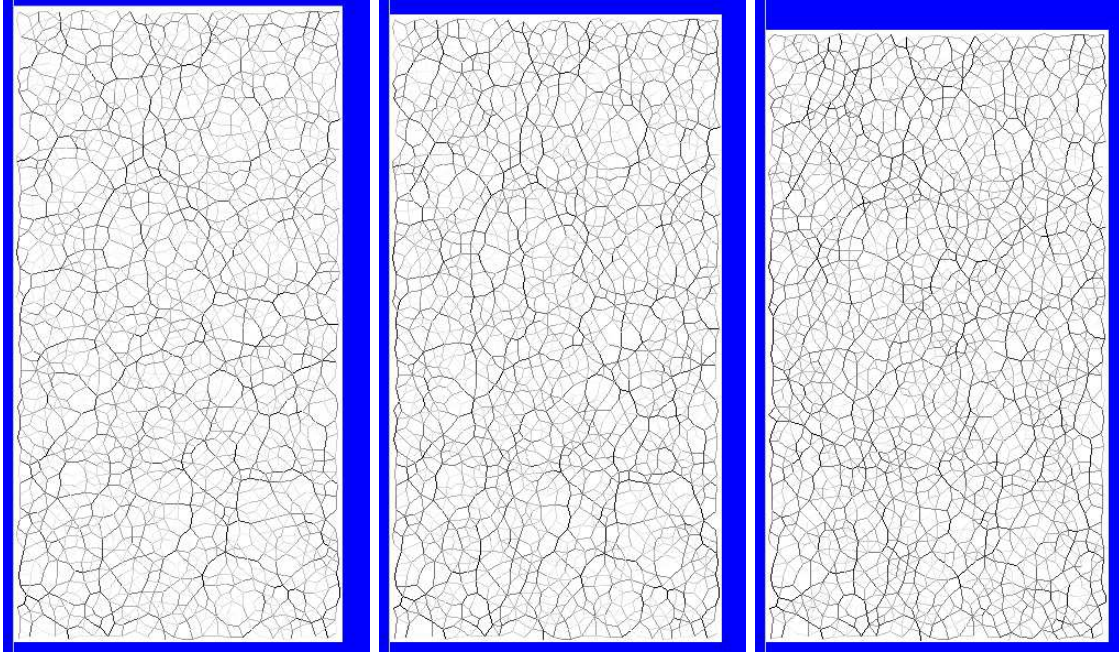


Figure 1.3: Contact networks for a typical simulation with $k_2 = 10^5 \text{ N m}^{-1}$, $k_1/k_2 = 1/2$, $k_c/k_2 = 2$, $\gamma_0 = 10^{-1} \text{ kg s}^{-1}$, $\gamma_b = \gamma_0/10$, and $\gamma_x = 193.5\gamma_0$. The grey-scale codes the strength of the contact force (dark lines correspond to strong forces) and the strain is (from left to right) $\varepsilon_{zz} = 0$, $\varepsilon_{zz} = 0.013$, and $\varepsilon_{zz} = 0.036$.

1.4.2 Relaxation

For some cases of isotropic relaxation, the final approach of stress to equilibrium is plotted in Fig. 1.4 for systems with $p = 400 \text{ N m}^{-2}$ and different parameters as discussed below. The unit of pressure is obtained by assuming that the system is extended in the third dimension for a length $h = 1 \text{ m}$. The pressure p_x exerted from the material on the right wall is then the sum over all forces divided by the wall-area $F_x/(hz)$. In the following, we present the pressure in these units, implying the h defined above as the system-extension in the third dimension. For a typical $z \approx 0.12 \text{ m}$, and assuming $N_x \approx 60$ contacts, one obtains an estimated mean overlap per particle $\delta_{\text{mean}} \approx phz/N_x k_1 = 1.6 \cdot 10^{-5} \text{ m}$.

In Fig. 1.4(a), the influence of the wall mass is examined for a system with standard γ_0 (see above) and no other dissipation $\gamma_x = \gamma_b = 0$. Weakly damped oscillations are obtained for rather large mass m_x , whereas the final pressure is rapidly approached for smaller mass, e. g. $m_x \leq 10^{-3} \text{ kg}$. Therefore, a small wall mass will be used in the following. However, a closer look at the approach to equilibrium leads to the conclusion that it is very slow. Therefore, we increase the dissipation in the spirit of faster relaxation.

One possible means of dissipation is the wall dissipation, γ_x . Small values of γ_x do not change the response as compared to Fig. 1.4(a). However, for larger values, a more complicated oscillation pattern is evidenced. Only for the largest $\gamma_x = 1935\gamma_0$, one can obtain sufficiently strong damping of the oscillation – but unfortunately on a rather long time-scale.

In order to achieve a more rapid approach to the final steady-state configuration, the (artificial) dissipation with the background is tuned on. For the combination of parameters, $m_x = 10^{-4}$ kg, $\gamma_x = 193.5\gamma_0$ and different γ_b , a rapid relaxation is obtained only for $\gamma_b \approx \gamma_0/10$, see Fig. 1.4(b). The time-scale of this exponential relaxation is $\tau \approx 0.0023$ s.

Having performed these test-simulations, we choose the parameters $m_x = 10^{-4}$ kg, $\gamma_x = 193.5\gamma_0$, and $\gamma_b = \gamma_0/10$ for the following simulations.

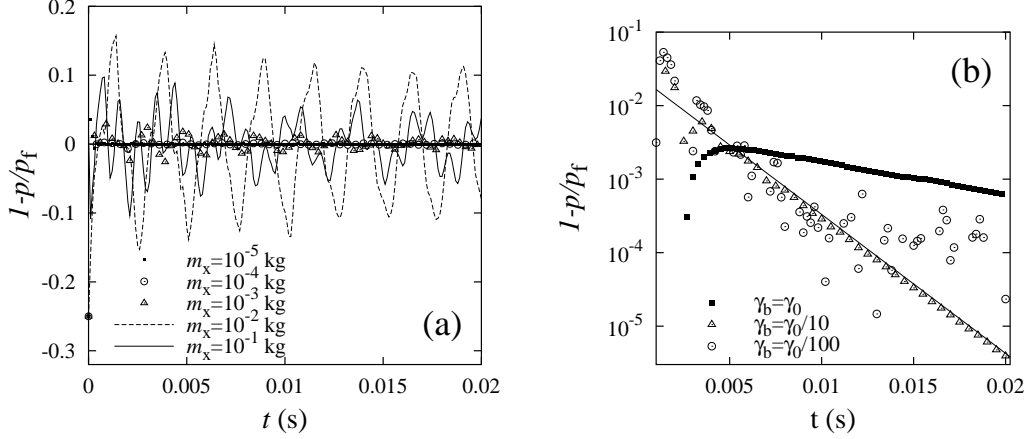


Figure 1.4: Approach to equilibrium pressure $p_f = 400$ for stiffness $k_2 = 10^5$ N m $^{-1}$, $k_1 = k_2/2$, $k_c = 0$, and contact dissipation $\gamma_0 = 0.1$ kg s $^{-1}$. (a) No additional dissipation $\gamma_b = \gamma_x = 0$, and different wall mass m_x as given in the inset. (b) Wall dissipation $\gamma_x = 193.5\gamma_0$ and different bottom dissipation γ_b as given in the inset for $m_x = 10^{-4}$ kg. The solid line indicates an exponential approach to equilibrium with relaxation time $\tau = 0.0023$ s. as given in the inset.

1.4.3 Rate-dependency

In Fig. 1.5, simulations with the same material parameters are presented, when a different rate of change of the position of the vertical wall is used, according to Eq. (1.1). The quantities examined are the volumetric strain, ε_V , the vertical stress σ_{zz} , the horizontal stress $\sigma_{xx} \approx p_x$, and the ratio of these stresses. The simulations show qualitatively similar behavior, only the strain and the stresses are higher for faster movement of the vertical wall. This is due to the artificial, velocity-dependent dissipation, see Eq. (1.9). With decreasing f , the simulation results almost coincide, only a tiny viscous stress remains in both directions. Note that the ratio of stresses σ_{zz}/σ_{xx} is not affected by the rate of deformation.

Since the error introduced by the artificial damping and the dynamic, strain-controlled set-up is well below 5 per-cent already for $f = 10$ s $^{-1}$, we use this frequency in the following, in order to save computing time. The strain of 3.5 per-cent is thus reached after $t \approx 0.05$ s, corresponding to several computing hours on a typical PC.

In the next subsection, we will use the fact that the stress ratio is not affected by the rate of deformation. From the horizontal stress we obtain the viscous over-stress $\sigma_{xx}^{\text{visc}} = \sigma_{xx} - p_x$,

and thus can obtain the corrected vertical stress using

$$\frac{\sigma_{zz}}{\sigma_{xx}} = \frac{\sigma_{zz}^{\text{corr}}}{p_x}, \text{ so that } \sigma_{zz}^{\text{corr}} = p_x \frac{\sigma_{zz}}{\sigma_{xx}}. \quad (1.10)$$

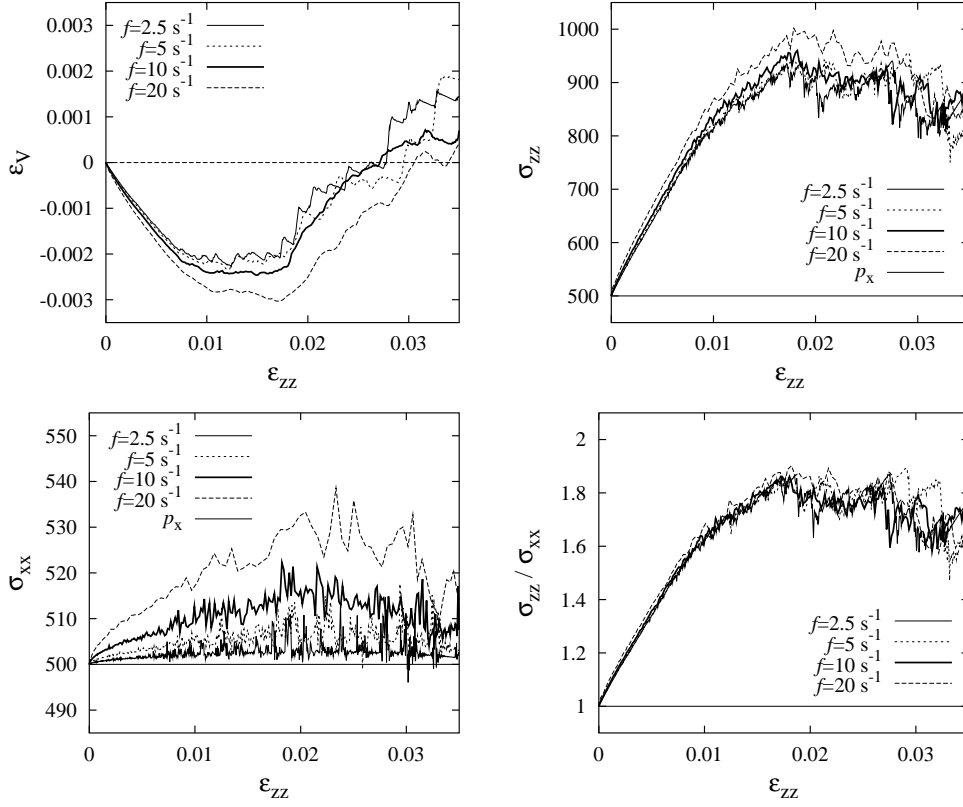


Figure 1.5: Simulation results from runs with $k_1 = k_2/2$, $k_c = 2k_1$, and different rate of compression f , as given in the inset. After initial compression, one obtains a smooth transition to a dilatant state with maximum, yield stress.

1.4.4 Measurement of the material parameters

The first series of simulations with varying cohesion strength k_c is performed at an initial pressure $p = 500$, see Fig. 1.6, the second series is performed at $p = 100$, see Fig. 1.7. For small strain ϵ_{zz} , the material is compressed, the change in density ϵ_V/ϵ_{zz} being larger for stronger cohesion k_c and smaller external pressure p . The initial negative slope can be identified with a function of the *Poisson-ratio* ν , from the relation $\epsilon_V/\epsilon_{zz} = \text{atan}(1 - 2\nu)$ [13], so that the simulations indicate $\nu \approx 0.66$.

When the upper wall moves further, dilatancy is evidenced at ϵ_{zz} -values between one and two per-cent for large external stress, but already for much smaller strain if the external pressure is smaller. The positive slope can be identified with the dilatancy function $d' = \text{atan} \frac{2 \sin \psi}{1 - \sin \psi}$ [13], with the *dilatancy angle* $\psi \approx 5^\circ$ for $p = 500$ and $\psi \approx 11^\circ$ for $p = 100$. The onset of dilatancy takes place before the maximum vertical stress is achieved and

thus before the failure of the material. The transition from the compressive to the dilatant regime is delayed to larger strain by stronger cohesion and stronger external pressure.

From the stress strain curves, one can extract the *Young modulus* E of the material from the slope of the initial increase of the vertical stress. From the simulation data, we evidence $E \approx k_1 = k_2/2$ at very small strain after the onset of the wall motion. For larger deformation, the slope and thus E decreases. After failure (see figures), softening is obtained for large p and weak cohesion, however, after further deformation, the material seems to reach a steady state. The maximum stress from each experiment is indicated by an arrow in the figures. Note that we use the maximum including fluctuations and not the maximum of the mean, fact which may lead to some overestimation.

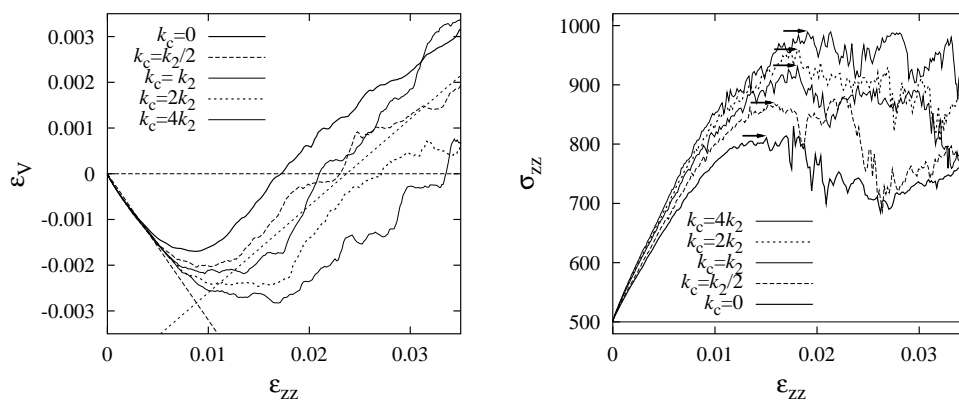


Figure 1.6: Simulation results from runs with $k_1 = k_2/2$, and different cohesion strength k_c , as given in the inset for $p_x = 500$. (Left) Volume change is plotted against ε_{ZZ} , and the straight lines indicate the slopes -0.32 and $+0.19$. (Right) Vertical stress σ_{ZZ} plotted against ε_{ZZ} ; the arrows indicate the peak-stress.

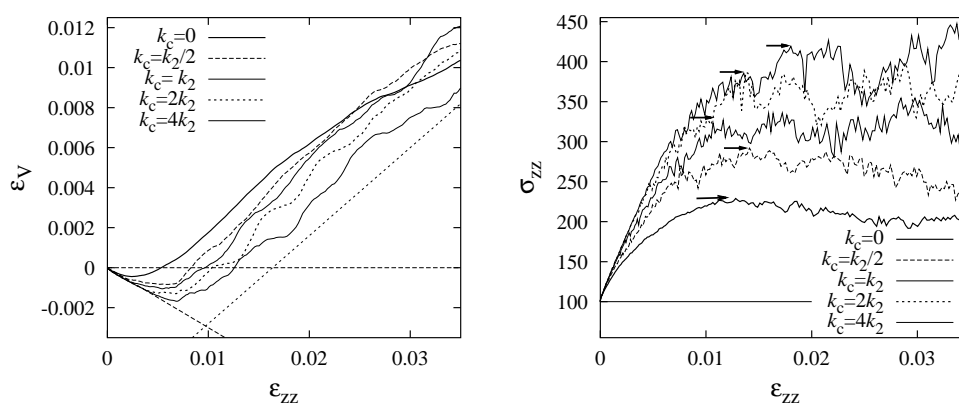


Figure 1.7: The same as in Fig. 1.6, only here $p_x = 100$, and the straight lines indicate the slopes -0.30 and $+0.44$.

1.4.5 Failure and Yield-Stress

Comparing the simulations with different densities, one obtains similar material parameters E and ν for different external stress. The different p , however, leads to stronger dilation for weak external stress and to stronger peak-stress at failure for larger external stress. Furthermore, the relative increase of the stress, i. e. σ_{zz}/p_x , is stronger for weak p , and, after failure, the cohesive material does not show clear softening behavior, only strong fluctuations can be observed for strong cohesion.

The yield-stresses from Figs. 1.6 and 1.7 are combined in Fig. 1.8 as Mohr-circles (where the corrected stresses, see Eq. (1.10), are used). Each set of Mohr circles corresponds to a fixed external pressure p and different circles correspond to different $k_c/k_2 = 0, 1/2, 1, 2,$ and 4 from the smallest to the largest circle. The tangent to a pair of circles with the same cohesion strength is plotted as a dotted line for all pairs. The slope of the lines is $\tan \phi \approx 0.23$ corresponding to an internal *friction angle* $\phi \approx 13^\circ$. Due to the absence of any friction in the model, ϕ has to be caused by the geometry of the packing which causes a shear resistance due to inter-locked particles.

The macroscopic *cohesion* c of the material can be obtained as the point of intersection of the dashed line and the zero vertical axis, as summarized in Table 1.1.

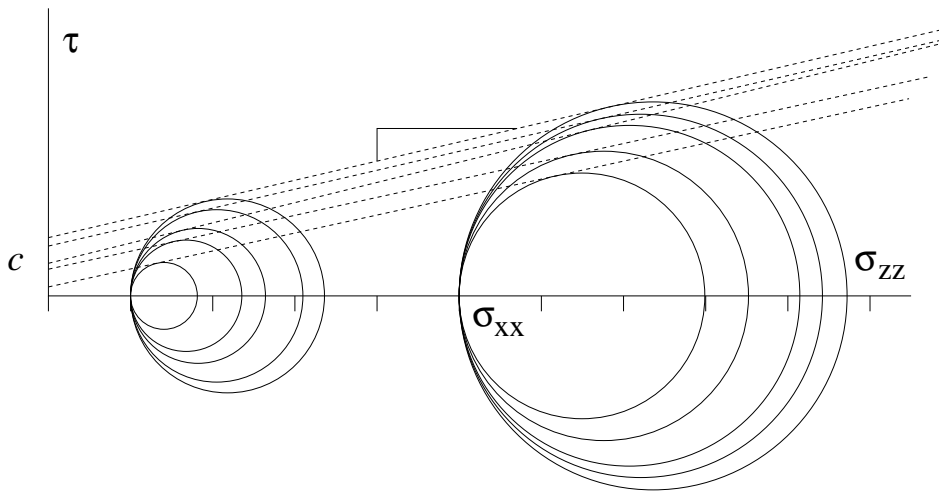


Figure 1.8: Mohr circles at failure, for the simulations in Figs. 1.6 and 1.7. The left end of the circle corresponds to the fixed pressure p_x , the right end to the corrected vertical pressure $\sigma_{zz}^{\text{corr}}$ at failure. The angle indicates a slope of about 0.23.

1.5 Summary and Conclusion

Using discrete element simulations of frictionless, cohesive granular material in a bi-axial box, the macroscopic material behavior was examined for different microscopic model parameters. The parameters under investigation were the Young modulus, the Poisson ratio, the dilatancy angle, the internal friction angle and the cohesion.

k_c/k_2	p_x	$\sigma_{zz}^{\text{corr}}$	p_x	$\sigma_{zz}^{\text{corr}}$	c
0	100	183	500	798	11
1/2	100	234	500	853	32
1	100	264	500	915	40
2	100	310	500	941	60
4	100	336	500	972	71

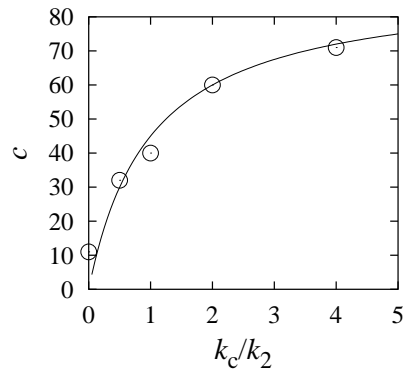


Table 1.1: Summary of the corrected peak-stress values and the corresponding cohesion c . The error for the stresses is about ± 3 , the error for c is about ± 10 . Note the artificially large c for $k_c = 0$, which we attribute also to the systematic error introduced by choosing the peak-stress as the maximum of the fluctuating data and not of some mean. The figure to the right shows the c -values as function of the cohesion strength, with the maximum attractive force $c \propto (k_2 - k_1)/(k_2 + k_c)$ given as solid line.

The interaction model can be seen as appropriate for rather small particles, where plastic deformations lead to the hysteretic response – for loading, the material behaves rather soft, whereas for unloading/reloading, the compressed contact area behaves more stiff. Due to its nature, the cohesive force depends on the maximum compression and is always recovered, i. e. the cohesive forces are reversible. Thus, the model seems appropriate for restorable cohesive forces, but not for damageable attraction like in e. g. concrete. For the latter, some damage parameter can be introduced in order to make the cohesion history dependent and unrecoverable.

During the strain controlled bi-axial test with fixed horizontal pressure, the material is first compressed, then starts to dilate and eventually yields at some peak-stress value. For strong external pressure, one obtains softening and, for weaker pressure, the vertical stress remains constant in a steady state, besides fluctuations. The material parameters from elasticity theory do not depend on the external pressure, but the dilatancy angle increases with decreasing external pressure. Even without microscopic friction, one obtains a macroscopic friction angle of the order of 13° . The macroscopic cohesion is proportional to the maximum attractive force in the microscopic model.

Future studies will involve microscopic friction and its effect on the material behavior. Furthermore, the preparation of the specimen before loading is started has to be defined in a more reproducible and history independent manner as in the present situation.

1.6 Acknowledgements

The authors thank M. Lätzel, J. Tomas, S. Diebels, H. Besserer, and G. A. D'Addetta for discussions and acknowledge financial support by the Deutsche Forschungsgemeinschaft (DFG).

Bibliography

- [1] Y. M. Bashir and J. D. Goddard. A novel simulation method for the quasi-static mechanics of granular assemblages. *J. Rheol.*, 35(5):849–885, 1991.
- [2] P. A. Cundall and O. D. L. Strack. A discrete numerical model for granular assemblies. *Géotechnique*, 29(1):47–65, 1979.
- [3] H. J. Herrmann, J.-P. Hovi, and S. Luding, editors. *Physics of dry granular media - NATO ASI Series E 350*, Dordrecht, 1998. Kluwer Academic Publishers.
- [4] S. Luding. Collisions & contacts between two particles. In H. J. Herrmann, J.-P. Hovi, and S. Luding, editors, *Physics of dry granular media - NATO ASI Series E350*, page 285, Dordrecht, 1998. Kluwer Academic Publishers.
- [5] S. Luding, E. Clément, A. Blumen, J. Rajchenbach, and J. Duran. Anomalous energy dissipation in molecular dynamics simulations of grains: The “detachment effect”. *Phys. Rev. E*, 50:4113, 1994.
- [6] S. Luding, E. Clément, A. Blumen, J. Rajchenbach, and J. Duran. The onset of convection in molecular dynamics simulations of grains. *Phys. Rev. E*, 50:R1762, 1994.
- [7] M. H. Sadd, Q. M. Tai, and A. Shukla. Contact law effects on wave propagation in particulate materials using distinct element modeling. *Int. J. Non-Linear Mechanics*, 28(2):251, 1993.
- [8] J. Schwedes. *Fließverhalten von Schüttgütern in Bunkern*. Verlag Chemie, Weinheim, 1968.
- [9] C. Thornton. Numerical simulations of deviatoric shear deformation of granular media. submitted to: *Géotechnique*, 1998.
- [10] C. Thornton and S. J. Antony. Quasi-static deformation of particulate media. submitted to: *Phil. Trans. Roy. Soc. A*, 1998.
- [11] Jürgen Tomas. Particle adhesion fundamentals and bulk powder consolidation. *KONA*, 18:157–169, 2000.
- [12] S. van Baars. *Discrete Element Analysis of Granular Materials*. PhD thesis, Technische Universiteit Delft, Delft, Netherlands, 1996.
- [13] P. A. Vermeer. Non-associated plasticity for soils, concrete and rock. In H. J. Herrmann, J.-P. Hovi, and S. Luding, editors, *Physics of dry granular media - NATO ASI Series E350*, page 163, Dordrecht, 1998. Kluwer Academic Publishers.
- [14] P. A. Vermeer, S. Diebels, W. Ehlers, H. J. Herrmann, S. Luding, and E. Ramm, editors. *Continuous and Discontinuous Modelling of Cohesive Frictional Materials*, Berlin, 2001. Springer. Lecture Notes on Physics 568.

- [15] O. R. Walton and R. L. Braun. Viscosity, granular-temperature, and stress calculations for shearing assemblies of inelastic, frictional disks. *Journal of Rheology*, 30(5):949–980, 1986.
- [16] C. Y. Zhu, A. Shukla, and M. H. Sadd. Prediction of dynamic contact loads in granular assemblies. *J. of Applied Mechanics*, 58:341, 1991.